FERMILAB-PUB-09-008-APC

submitted to HB2008 PRST-AB Special Edition

Simulations of beam-beam and beam-wire interactions in RHIC

Hyung J. Kim* and Tanaji Sen
Fermi National Accelerator Laboratory, Batavia, Illinois 60510, USA

Natalia P. Abreu and Wolfram Fischer
Brookhaven National Laboratory, Upton, NY 11973, USA

The beam-beam interaction is one of the dominant sources of emittance growth and luminosity lifetime deterioration. A current carrying wire has been proposed to compensate long-range beam-beam effects in the LHC and strong localized long-range beam-beam effects are experimentally investigated in the RHIC collider. Tune shift, beam transfer function, and beam loss rate are measured in dedicated experiments. In this paper, we report on simulations to study the effect of beam-wire interactions based on diffusive apertures, beam loss rates, and beam transfer function using a parallelized weak-strong beam simulation code (`BBSIMC`). The simulation results are compared with measurements performed in RHIC during 2007 and 2008.

PACS numbers: 29.20.db, 29.27.Bd

I. INTRODUCTION

Long-range beam-beam interactions are known to cause emittance growth or beam loss in the Tevatron [1, 2] and are expected to deteriorate beam quality in the LHC. A possible remedy to reduce their effects is to increase the crossing angle. However, it has a side effect of reducing the luminosity due to the reduction in geometric overlap. Compensation of long-range beam-beam interactions by applying external electromagnetic forces has been proposed for the LHC [3]. At large beam-beam separation, the electromagnetic force which a beam exerts on individual particles of the other beam is proportional to $\frac{1}{r}$, which can be generated and canceled out by the magnetic field of a current-carrying wire. Direct-current wires were installed in SPS [4], DAΦNE [6], and later in RHIC [7] for tests. Results of the SPS wire excitation experiments have been reported earlier [5, 8]. During the KLOE experiment in DAΦNE, an improvement of beam lifetime without luminosity loss due to the compensation of parasitic collisions has been observed [6]. Experiments in RHIC supplement the SPS and DAΦNE tests. The beam lifetime in RHIC is typical for a collider storage ring and better than in the other two machines. Unlike the SPS, two beams circulate and interact in RHIC and compensation of a single long-range interaction is possible. The energies and other beam conditions are also different from the SPS and DAΦNE. So the results reported here will result in simulations being benchmarked under a wider range of operating conditions.

Two current carrying wires, one for each beam, have been installed between the magnets $Q3$ and $Q4$ of IP6 in the RHIC tunnel. Their impact on a beam was measured during the physics run with deuteron and gold beams. No attempt was made to compensate the beam-beam interaction since so far only ion beams were available which have a beam-beam parameter about a factor of 3 smaller than proton beams. However, the experimental results help to understand the beam-beam effects because the wire force is similar to the long-range beam-beam force at large separations. In this report we discuss the results of numerical simulations of a wire acting on a beam in RHIC using a multi-particle tracking code and compare with measurements in RHIC Run 7 and 8 [9].

The organization of the paper is as follows: The physical models used in the simulation code are described in Section II. The beam and wire parameters are given in Section III. Section IV presents the simulation results of the effects of the wire on the beam dynamics and the comparison between measurement and simulation results. We summarize our results in Section V.

II. MODEL

In the collider simulation, the two beams moving in opposite direction are represented by macroparticles of which the charge to mass ratio is that of each beam. The number of macroparticles is much less than the bunch intensity of the beam because even with modern supercomputers it is too time consuming to track 10^{11} particles for the number of revolutions of interest. The macroparticles are generated and loaded with an initial distribution for a specific simulation purpose, for example, six-dimensional Gaussian distribution for long-term beam evolution. The transverse and longitudinal motion of particles is calculated by transfer maps which consist of linear and nonlinear maps. In the simulations, the following nonlinearities are included: head-on and long-range beam-beam interactions, external electromagnetic force by current carrying wire, multipole errors in the interaction region (IR) quadrupole triplets, and sextupoles for chromaticity correction. The finite bunch length effect of the beam-beam interactions is considered by slicing the beam into several sections in the longitudinal direction and by a synchro-

*Electronic address: `hjkim@fnal.gov`; URL: `http://www-ap.fnal.gov/~hjkim`

beam map [10]. Each slice in a beam interacts with particles in the other beam in turn at the collision points. In addition, the magnetic field of a finite length of wire is calculated using the Biot-Savart law at the particles' betatron amplitude.

The six-dimensional accelerator coordinates $\mathbf{x} = \left(x, x^{'}, y, y^{'}, z, \delta\right)^T$ are applied, where x and y are horizontal and vertical coordinates, $x^{'}$ and $y^{'}$ the trajectory slopes of each coordinates, $z = -c\Delta t$ the longitudinal distance from the synchronous particle, and $\delta = \Delta p_z/p_0$ the momentum deviation from the synchronous energy. Coupling between the transverse planes is included in the transfer map between elements. We adopt the weak-strong model to treat the beam-beam interactions where one beam is strong and is not affected by the other beam while the other beam is weak and experiences a beam-beam force due to the strong beam during the interactions. The density distribution of the strong beam is assumed to be Gaussian.

It is well known that for a large separation distance ($\gg \sigma$) at parasitic crossings, the strength of long-range interactions is inversely proportional to the distance. Its effect on a test beam can be compensated by current carrying wires which create just the $\frac{1}{r}$ field. The advantage of such an approach consists of the simplicity of the method and the possibility to deal with all multipole orders at once. For a finite length of a wire embedded in the middle of a drift length L and tilted in pitch and yaw angles, the transfer map of a wire can be written as [11]

$$\begin{aligned}\mathcal{M}_w = S_{\Delta x,\Delta y} \odot T^{-1}_{\theta_x,\theta_y} \odot D_{L/2} \odot \mathcal{M}_k \\ \odot D_{L/2} \odot T_{\theta_x,\theta_y},\end{aligned} \tag{1}$$

where T_{θ_x,θ_y} represents the tilt of the coordinate system by horizontal and vertical angles θ_x, θ_y to orient the coordinate system parallel to the wire, $D_{L/2}$ is the drift map with a length $\frac{L}{2}$, $\mathcal{M}_k$ is the wire kick integrated over a drift length, and $S_{\Delta x,\Delta y}$ represents a shift of the coordinate axes to make the coordinate systems after and before the wire agree.

At the start of the simulation, the particles in the weak beam are distributed over the phase space $\mathbf{x} = \left(x, x^{'}, y, y^{'}, z, \delta\right)^T$. The number of particles N is limited by the computational power. In order to make the best use of a relatively small number of simulation particles compared to the bunch intensity, the initial distribution should be optimized. Indeed the initial distribution is very important because a proper choice can reduce the statistical noise in the physical quantities. The simulation particles are generated in two steps: (i) The particle coordinates (x, y, z) of particles can be directly generated from the spatial Gaussian distribution, $\bar{\rho}\left(x, y, z\right) = \bar{\rho}_x\left(x\right)\bar{\rho}_y\left(y\right)\bar{\rho}_z\left(z\right)$, where $\bar{\rho}_\zeta\left(\zeta\right) = \bar{\rho}_{\zeta 0}\exp\left(-\frac{\zeta^2}{2\sigma_\zeta^2}\right)$. Since the particle coordinates are not correlated, one can generate them by inverse mapping of each cumulative distribution function of horizontal, vertical, and longitudinal Gaussian distributions, using bit-reversed sequence to minimize nonphysical correlations [12]. (ii) An equilibrium distribution in transverse phase space e.g. in the (x, x') plane is $\hat{\rho}\left(x, x^{'}\right) = \hat{\rho}_0\exp\left(-\frac{x^2+\left(\beta_x x^{'}+\alpha_x x\right)^2}{2\sigma}\right)$. Since the spatial coordinate x is determined at the first step, the slope $x^{'}$ can be obtained from the random variate r of a univariable Gaussian, i.e., $x^{'} = \left(r - \alpha_x x\right)/\beta_x$.

Following the above physical model, a beam-beam simulation code `BBSIMC` has been developed at FNAL over the past few years to study the effects of the machine nonlinearities and the beam-beam interactions [13]. If required, time dependent effects such as tune modulation and fluctuation, beam offset modulation and fluctuation, dipole strength fluctuations to mimic rest-gas scattering etc can be included in the model. The code is under continuous development with the emphasis being on including the important details of an accelerator and the ability to reproduce observations in diagnostic devices. At present, the code can be used to calculate tune footprints, dynamic apertures, beam transfer functions, frequency diffusion maps, action diffusion coefficients, emittance growth and beam lifetime. Calculation of the last two quantities over the long time scales of interest is time consuming even with modern computer technology. In order to run efficiently on a multiprocessor system, the resulting model was implemented by using parallel libraries which are MPI (interprocessor Message Passing Interface standard) [14], state-of-the-art parallel solver libraries (Portable, Extensible Toolkit for Scientific Calculation, PETSc) [15], and HDF5 (Hierarchical Data Format) [16].

III. WIRE AND BEAM PARAMETERS

The transverse electric field of a round Gaussian bunch with transverse rms size σ is

$$\vec{E} = \frac{n_* q_*}{2\pi\epsilon_0}\frac{\vec{r}}{r^2}\left[1 - \exp\left(-\frac{r^2}{2\sigma^2}\right)\right], \tag{2}$$

where n_* and q_* are the number of particles and the electric charge in the opposite bunch respectively, and r is the radial distance from the center of the beam. At a small radius $r \ll \sigma$, the field is proportional to r and shifts the betatron tune. This tune shift is characterized by the beam-beam parameter $\xi = \frac{n_* r_0}{4\pi\epsilon}$, where r_0 is the classical radius of the particle, $\epsilon = \gamma\sigma^2/\beta^2$ is the normalized emittance. While particles at small r undergo a linear tune shift, the particles with $r \gg \sigma$ experience a $\frac{1}{r}$ force. The long-range effect is nonlinear and may vary from bunch to bunch if the the bunch pattern is asymmetric. A current carrying wire generates a magnetic force which is $\propto \frac{1}{r}$, the same as the long-range beam-beam force at large separations. The wire current required to compensate a long-range interaction is $(I_w L_w) = n_* q_* c$, where I_w is the wire current, and L_w its length. In addition to the wire strength, the phase advance from the

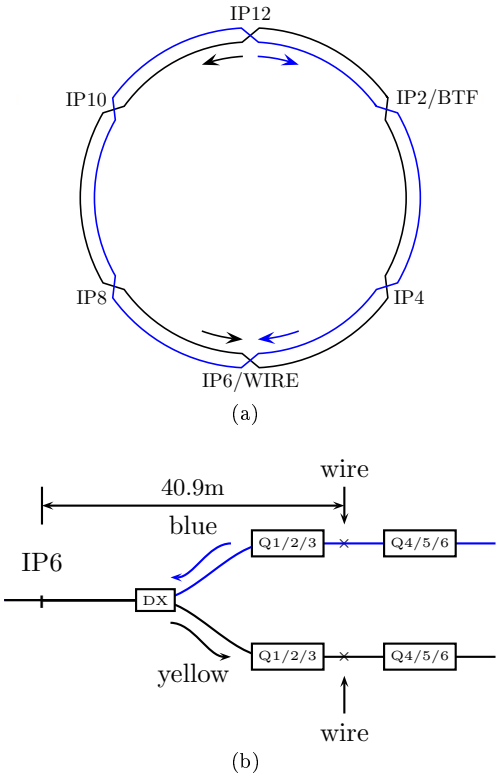

Figure 1: (a) Layout of RHIC, and (b) location of the long-range beam-beam interaction and wire compensators at IP6. Beam-beam collisions occur at IP6 (STAR) and IP8 (PHOENIX).

location of the wire to the location of the long-range interaction should be small for an effective compensation of the long-range interaction [17]. In RHIC, a possible parasitic collision point is near the separation DX dipole magnets near IP6 and IP8. There is sufficient space in the straight sections between quadrupoles Q_3 and Q_4 for the wires. The phase advance between the DX magnet and the wire location is 5.7° for $\beta^* = 1$ m and is expected to provide effective compensation [18].

Figure 1 (a) shows the overall layout of RHIC which has two head-on beam-beam collisions at IP6 and IP8. The Yellow beam revolves in a counter clockwise direction, and the Blue beam revolves clockwise. The elements and the location of the wire at IP6 are shown in Fig. 1 (b). Two wires are currently installed in RHIC: one for each beam. In these simulations the effects of a current carrying wire on a beam have been studied for different RHIC runs: gold beam at both injection and store energies, and deuteron beam at store energy. The parameters of RHIC used in our simulations are shown in Table I. The length of each wire is 2.5 m. The wire current can be varied to a maximum of 50 A. Each wire can be moved in the vertical direction over a range of 65 mm.

IV. EFFECTS OF A WIRE ON A BEAM

The integrated magnetic fields $\vec{B}$ from a wire are found from [11]

$$\begin{pmatrix} B_x \\ B_y \end{pmatrix} = \frac{\mu_0 I_w}{4\pi} \frac{u - v}{x^2 + y^2} \begin{pmatrix} x \\ y \end{pmatrix}, \tag{3}$$

where I_w is the current of wire compensator, u and v are $\sqrt{\left(\frac{3L_w}{2}\right)^2 + x^2 + y^2}$ and $\sqrt{\left(\frac{L_w}{2}\right)^2 + x^2 + y^2}$ respectively, and L_w the length of the wire. For the wire kick, the the field and the force exerted on the beam are $\propto 1/r$ where r is the transverse distance from the beam to the wire. This force is nonlinear and is expected to have a significant impact on the beam quality at sufficiently close distances.

The impact of a wire can be observed in RHIC by measuring the orbit change, tune shift, the beam transfer function and the loss rates. The tune shift is one of the fundamental observables and it can be directly verified with analytical calculation. However, numerical simulations allow us to calculate other quantities not easily observable but which give valuable insight into the beam dynamics and can complement the experiments. These numerically calculable quantities include the tune footprint, the frequency diffusion map, the dynamic aperture, and the diffusion coefficients to characterize the diffusion in action. In this section, we present the simulation results of all the above quantities at RHIC injection and collision runs, and compare them to measurements where possible.

In the model for dynamics at injection energy we include the chromaticity sextupoles, these being the dominant nonlinearity, and the current carrying wire. It should be noted that the persistent current sextupoles in the arc dipoles were not included in the model because their inclusion would have increased the computation time substantially and they have a smaller impact on the dynamics compared to the chromaticity correcting sextupoles. At collision energy, the beam is strongly influenced by both machine nonlinearities and beam-beam interactions. In the collision model, we include the chromaticity sextupoles, the nonlinear field errors in the IR triplets, and the head-on beam-beam interactions at IP6 and IP8, together with the wire. There are two variables associated with the wire that can be varied: the wire current and the beam-wire separation. In the simulations the wire strength is set to the maximum value of 125 Am in the RHIC wire compensator so that the effects due to the wire may be clearly evident. These results will be compared with the data taken at this current during the machine experiments of 2007 and 2008. Depending on the purpose of the simulation, the beam-wire separation is also varied typically in the range of 4-10 σ where σ is the rms beam size at the wire location. The beam-wire separation is only in the vertical direction. The Blue wire is placed below, the Yellow wire above the beam. The simulations reported here will be for the Blue beam.

quantity	unit	gold beam		deuteron beam
		injection	store	
energy	Gev/nucleon	9.795	100	107.396
bunch intensity (Blue/Yellow)	10^9	0.7/0.7	1/1	134/1
emittance $\epsilon_{x,y}(95\%)$	mm mrad	5.8	18	17
(β_x^*, β_y^*) at IP6	m	(9.93, 10.0)	(0.97, 0.94)	(0.87, 0.89)
(β_x, β_y) at wire location	m	(119.7, 34.6)	(1082, 392)	(1194, 393)
beam-beam parameter ξ	10^{-3}		1.25	1.46
revolution frequency	kHz	77.8	78.2	78.2
tunes (ν_x, ν_y): Blue		(0.230, 0.216)	(0.220, 0.231)	(0.235, 0.225)
tunes (ν_x, ν_y): Yellow		(0.220, 0.230)	(0.232, 0.228)	(0.225, 0.235)
chromaticity (ξ_x, ξ_y)		(2, 2)	(2, 2)	(2, 2)
$(IL)_{max}$	Am		125	
L_w	m		2.5	
r_w	mm		3.5	
vertical separation (d_y)	σ	7-14	6-10	7-12

Table I: RHIC parameters for gold beam at injection and store, and deuteron beam at store.

A. Tune shift and tune footprint

A basic check of the simulation is to compare the simulated tune shifts with the measured tune shifts and also against analytical calculation. The transverse tune shift at zero amplitude due to wire kicks is given by

$$\Delta\nu_{x,y} = \pm\frac{\mu_0 I_w L_w}{8\pi^2 (B\rho)\,\sigma^2}\beta_{x,y}\frac{d_y^2 - d_x^2}{\left(d_y^2 + d_x^2\right)^2}, \qquad (4)$$

where $d_{x,y}$ denote the beam-wire distances normalized by $\sigma_{x,y}$, the rms beam sizes at the wire location, $I_w L_w$ the integrated strength of the wire, and $\beta_{x,y}$ the beta functions at wire location. At the wire location, the ratio of horizontal to vertical beta functions is $\beta_x/\beta_y = 2.8$ for the gold beam at store, and $\beta_x/\beta_y = 3.0$ for the deuteron beam. For $I_w L_w = 125$ Am which is the maximum integrated strength allowed in the RHIC wire installation, we get the horizontal tune shifts at 7 σ vertical separation: $\Delta\nu_x = 5.1 \times 10^{-3}$ for the gold beam, and $\Delta\nu_x = 5.9 \times 10^{-3}$ for the deuteron beam at store. Without the wire, beam-beam collisions are a major source of tune spread and shift. The beam-beam parameters for two head-on collisions are $\xi = 2.4 \times 10^{-3}$ and $\xi = 2.8 \times 10^{-3}$ for gold and deuteron beams at store energy respectively. These tune shifts are calculated for zero amplitude particles. For beam-wire separations greater than 6 σ, the large amplitude particles experience a detuning and shift mainly from the wire while the tune shift of small amplitude particles is dominated by the head-on collisions.

In our simulations, particle tunes are calculated with a Hanning filter applied to an fast-Fourier transform of particle coordinates found from tracking. Figure 2 (a) compares the analytical expression in Eq. 4 with the tune shift from tracking and averaged over a Gaussian distribution of particles. The changes in the transverse tune as a function of the beam-wire vertical separation distance in units of σ_y is in good agreement with the analytic relation Eq. 4. The relative difference in vertical

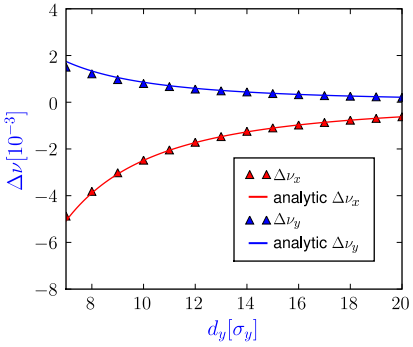

(a)

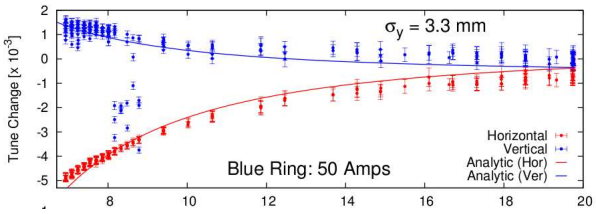

(b)

Figure 2: Plots of tune shift dependence on the wire separation distance: (a) simulation and (b) measurement [7]. Data sets are obtained at gold beam at store energy.

tune shift between the simulation and theory is $\approx 10\%$ at $d_y = 7$ σ, which stems from our usage of the centroid to calculate the tune shift and not the zero amplitude particle. The measured tune shifts in the recent experiments are compared with the analytical values in Fig. 2(b). These show that measurements and simulations also agree.

The tune footprint also provides useful information especially on the choice of working point and in finding the resonances spanned by the beam distribution. Figure 3 shows tune footprints from tracking single particles with

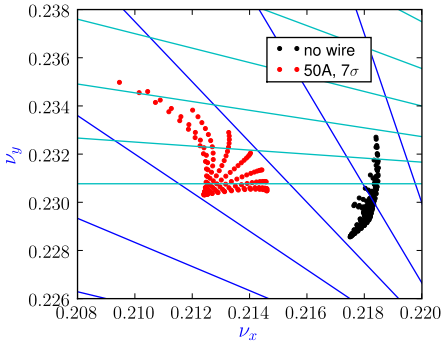

(a)

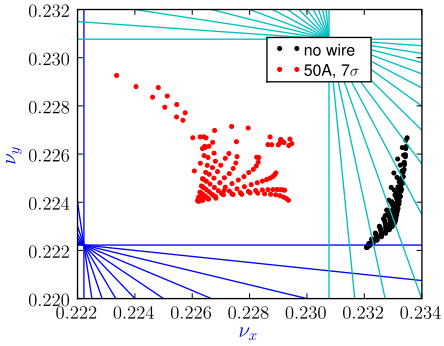

(b)

Figure 3: Plots of tune footprints for (a) gold beam and (b) deuteron beam at store energy. The no-wire case includes sextupoles, IR multipoles, and head-on collisions. The wire current is 50A and wire-beam separation distance sets to 7σ. Blue and cyan lines stand for 9^{th} and 12^{th} order resonances respectively.

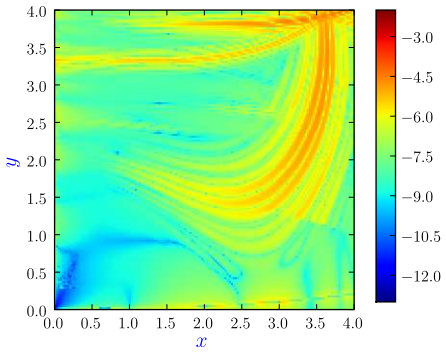

(a)

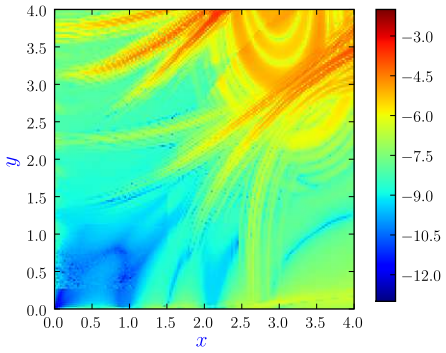

(b)

Figure 4: Plot of frequency diffusion map of betatron tunes (a) without and (b) with wire for gold beam at collision energy. Wire strength is 125 Am, and wire-beam separation is 7σ. The tune change is logarithmically scaled by $\log\sqrt{\Delta\nu_x^2+\Delta\nu_y^2}$.

initial amplitudes in the range 0-4 $\sigma_{x,y}$ for two cases: without the wire and with the wire powered at 125 Am and 7σ vertical separation from the beam. Comparing the two footprints without and with the wire, we observe that the horizontal tune shift due to the wire is different from the vertical one. The ratio of horizontal to vertical tune shifts is, for example, $\Delta\nu_x/\Delta\nu_y = 2.8$ for the gold beam, as shown in Fig. 3 (a), which agrees well with the ratio of beta functions at the wire. We observe that the width of the footprint is wider at large amplitude due to its dependence on the separation distance between a target particle and the wire. The wire alone causes the horizontal tune spread, for example, at 4 σ amplitude to be 10 times larger than for the no wire case. Characteristics of tune footprints of the deuteron beam, seen in Fig. 3 (b), are similar to that of the gold beam. However, the final tunes of the deuteron beam due to the wire is closer to the diagonal than the gold beam tunes due to the difference of their nominal tunes. Both the 9^{th} and 12^{th} order resonances are spanned by the gold beam while the deuteron beam is free from these resonances. The tune shifts are slightly larger for the deuteron beam than the gold beam because of the difference of beta functions and beam sizes.

B. Frequency diffusion

We have calculated frequency diffusion maps as another way to investigate the effects of a current carrying wire. The map represents the variation of the betatron tunes over two successive sets of the tunes [19]: The variation can be quantified by $d = \log\sqrt{\Delta\nu_x^2+\Delta\nu_y^2}$, where $\Delta\nu_x = \nu_x^{(2)} - \nu_x^{(1)}$ is the horizontal tune variation, in the simulations, between the first set of 1024 turns and the next set of 1024 turns, and $\Delta\nu_y = \nu_y^{(2)} - \nu_y^{(1)}$. If the tunes $\left(\nu_x^{(1)}, \nu_y^{(1)}\right)$ are different from $\left(\nu_x^{(2)}, \nu_y^{(2)}\right)$, the particle's orbit diffuses. A large tune variation is generally an indicator of reduced stability.

Figure 4 shows the frequency diffusion map of the betatron tune for the gold beam at collision energy and the influence of the wire on the map. The color scale shown

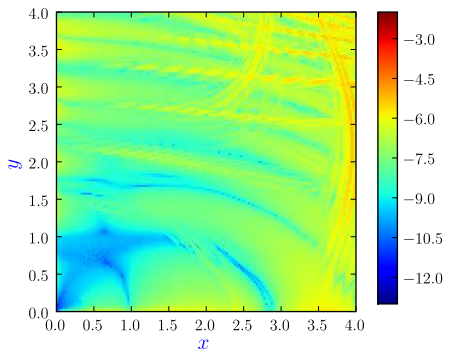

(a)

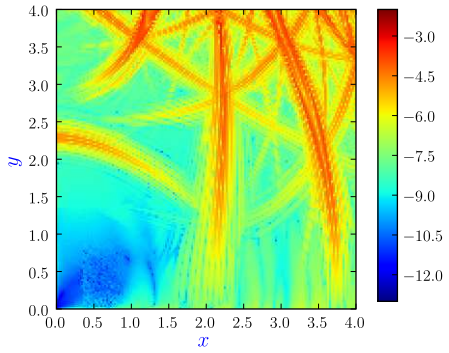

(b)

Figure 5: Plot of frequency diffusion map of betatron tunes (a) without and (b) with wire for deuteron beam at collision energy. Wire strength is 125 Am, and wire-beam separation is 7 σ. The tune change is logarithmically scaled by $\log\sqrt{\Delta\nu_x^2 + \Delta\nu_y^2}$.

on the right of each map gives a quantitative measure of the diffusion: red color corresponds to larger diffusion, and blue color represents less diffusion. In Fig. 4 we directly see the lines connected to resonances. The wire increases the detuning of betatron tune and makes the particle motions more chaotic at amplitude beyond 3 σ. The stability boundary is shrunk further. The diffusion map, Fig. 5 (a), of the deuteron beam without the wire shows mostly stable motion and only a small region with appreciable diffusion. It doesn't show the traces of resonances and looks quite different from that of the gold beam. This is to be expected since the resonances spanning the footprint of the deuteron beam are only 12^{th} order. However, the wire changes the diffusion map significantly, as is evident in Fig. 5 (b). While the region of high diffusion for the gold beam is distributed at large amplitudes, the regions with large diffusion are observed even at small amplitudes with the deuteron beam. The red "tongues" even extend to particles in the core, e.g. to particles at 0.5 σ. This is to be contrasted with the tune footprint in Fig 3 which shows that no resonances below 12th order are spanned by the beam distribution. In later sections we will discuss the correlation of these frequency diffusion maps with the dynamic aperture and loss rates.

C. Dynamic Aperture

Magnet nonlinearities and beam-beam interactions limit the dynamic aperture. The dynamic aperture quantifies detrimental effects of nonlinearities and can be calculated relatively quickly. The dynamic aperture of an accelerator is defined as the largest radial amplitude of particles that survive up to a certain time interval; in this simulation, we choose 10^6 turns for both injection and collision which corresponds to 13 seconds circulation time in RHIC. It is, for example, only about 10% of the RHIC injection period for ions. We examined the dependence of the aperture on the number of turns by calculating it for $10^4 - 10^7$ turns and found that the dynamic aperture stays nearly constant after 10^6 turns.

We have seen that a wire has a significant impact on the tune shift and tune spread, for example, the tune shift due to 125 Am wire strength is 0.005 at 7 σ separation. The significant increase of the frequency diffusion due to the wire implies that the motion of particles becomes more chaotic at large amplitudes. Hence we can expect that a wire will also have a significant impact on the dynamic aperture.

At injection energy the simulation model for dynamic aperture calculations includes sextupoles, transverse coupling, as well as the nonlinearity due to the wire. At collision energy, the nonlinearities due to the multipoles in the IR quadrupoles are added and the head-on beam-beam interactions. Particles are distributed uniformly over the transverse planes with amplitudes 0-15 σ. The linear chromaticity is set $(\xi_x, \xi_y) = (+2, +2)$. Since non-zero chromaticity increases the momentum dependent tune spread, the off-momentum particles cross more betatron resonances during synchrotron oscillations. The plots in Fig. 6 show the dynamic aperture for the gold beam at injection energy, the gold beam at collision energy and the deuteron beam at collision energy respectively. Plots (a) and (b) in Fig. 6 show that nonlinearities of the IR triplets play a major role in determining the stability boundary. When the electromagnetic force due to the wire is not present, the boundary at injection energy is at 15 σ while this boundary at collision energy falls to 7 σ primarily due to the IR multipole errors. The effect of the head-on beam-beam collisions on the dynamic aperture is negligible over our simulation period since the head-on interactions do not transport particles to large amplitudes. Sextupoles have only a small impact at collision energy since their strengths are relatively small compared to the IR multipole strengths. The stability boundaries are approximately circular, but the wire distorts the boundaries near the vertical plane since the beam-wire separation is entirely in the vertical plane. The dynamic aperture near the vertical plane decreases considerably as the wire ap-

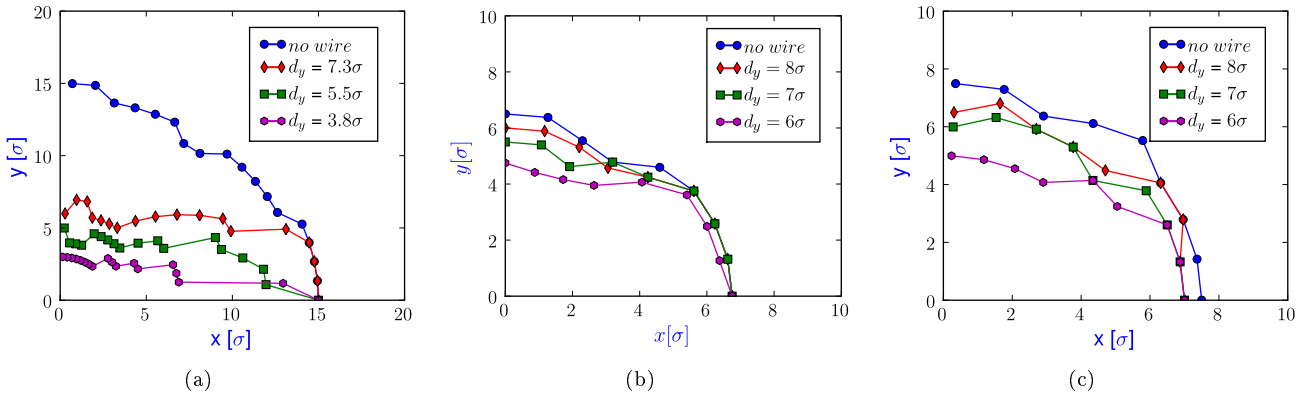

Figure 6: Plots of dynamic aperture according to wire separation distance: (a) gold beam injection energy, (b) gold beam collision energy, and (c) deuteron beam collision energy. The wire strength is set 125 Am.

proaches the beam. The stability boundary along the vertical plane is directly proportional to the wire separation while along the horizontal plane, the boundary is nearly independent of the separation. The difference in the dynamic aperture between the deuteron beam and the gold beam at collision energies is approximately 1 σ when the wire is not present. This can be understood from the difference in resonances spanning between both beams mentioned in the previous section. With the wire powered, the dynamic aperture in the two cases is nearly the same.

We now turn to tune scans of the dynamic aperture. One of the key parameters for machine operation is the working point. The search for a working point with a good beam lifetime and high luminosity is always a major issue. Since the dynamic aperture becomes smaller when the betatron tune of beam particles is on or across resonances, the tune diagram is often a useful indicator of single particle stability. In the simulations, the tune scans are performed with increments of $\Delta\nu = 0.01$ in the two transverse directions. At each set of the tune scan, we load identical distributions in order to avoid the uncertainties due to different distribution and beam size reduction from the previous tune.

Figure 7 shows the contour plots of dynamic apertures over transverse tunes for two different wire separations for gold injection energy. Red indicates low dynamic apertures around 3 σ while blue indicates high dynamic apertures around 11 σ. It is found that at all wire separations, the largest dynamic apertures are distributed along a band parallel to the diagonal, i.e., $\nu_x - \nu_y \simeq 0.02$. On the other hand, the zone along $\nu_x - \nu_y \simeq 0.03$ has the smallest dynamic apertures at all separations. This scan indicates that the nominal tune $(28.230, 29.216)$ is close to optimal. Furthermore, a sharper drop in dynamic aperture is observed near the 5^{th} resonances than at other resonances as the separation decreases from 8 σ to 4 σ. Figure 8 shows the dynamic apertures over transverse tunes for gold collision energy. Here red stands for 5 σ while blue for 11 σ. Since the IR multipoles cause a large drop in dynamic aperture at collision energy and the wire has a relatively smaller effect, we exclude the IR multipole errors in order to see the effect of the wire alone. As expected, the smallest dynamic aperture is observed near 4^{th} and 5^{th} resonances. At all wire separations, the largest dynamic apertures are distributed nearly along the diagonal between $\nu_x = 0.21$ and $\nu_x = 0.24$. The effect of the wire on the dynamic aperture of the deuteron beam is presented in Fig. 9. It is clear that the reduction of the dynamic aperture is dominant near 4^{th} resonance. A notable variation is seen near a circular band, i.e., $\nu_x^2 + \nu_y^2 \simeq 0.21^2$, when the beam-wire separation is small, while the circular band is not detected in the gold beam. Indeed, the large stability boundary is distributed all over the tune space except the particular bands. Since the wire kick at a large separation is equivalent to long-range beam-beam interaction, these scans can be interpreted as showing the effects of a long-range interaction at different tunes.

D. Beam Transfer Functions

The beam transfer function (BTF) is defined as the beam response to a small external longitudinal or transverse excitation at a given frequency. BTF diagnostics are widely employed in modern storage rings due to its non-destructive nature. The beam response is observed usually in a downstream pickup while either a stripline kicker or RF cavity excites the betatron or synchrotron oscillation over the tune spectrum. The fundamental applications of BTF are to measure the transverse tune and tune distribution by exciting betatron oscillation, to analyze the beam stability limits, and to determine the impedance characteristics of the chamber wall and feedback system [20–22]. Since this is one of the observables in RHIC, we calculate the BTF to benchmark another output from the code against measurements.

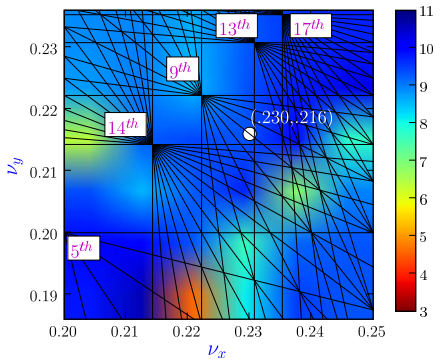

(a)

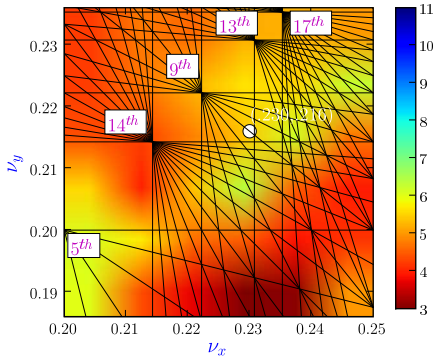

(b)

Figure 7: Tune scan of dynamic aperture at gold injection energy: (a) $d_y = 7.8\sigma$ and (b) $d_y = 3.8\sigma$. Working point $(28.230, 29.216)$ is plotted as a white dot. Red indicates low dynamic apertures while blue indicates high dynamic apertures. The unit of dynamic aperture is σ.

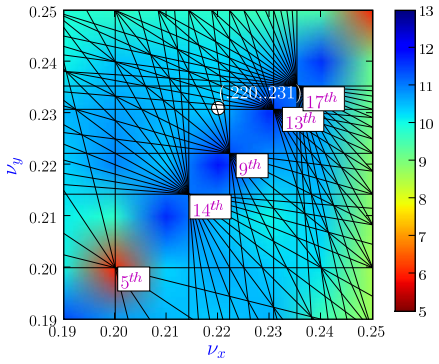

(a)

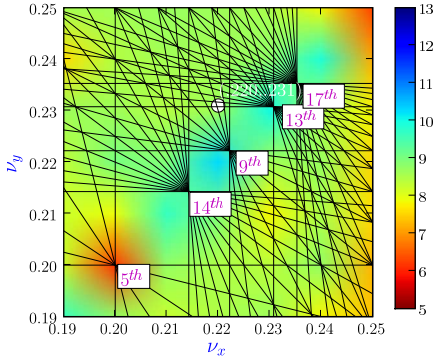

(b)

Figure 8: Tune scan of dynamic aperture at gold collision energy: (a) $d_y = 8\ \sigma$ and (b) $d_y = 6\ \sigma$. Working point $(28.220, 29.231)$ is plotted as a white dot. Red indicates low dynamic apertures while blue indicates high dynamic apertures. The unit of dynamic aperture is σ.

Figure 10 presents the beam transfer functions for deuteron collision energy and nominal tune $(28.228, 29.225)$ obtained by applying a sinusoidal driving force to a beam in transverse plane and tracking the excited particles over 1024 turns at each excitation frequency of the kicker. The driving frequency is swept from $(n + 0.21)\, f_{rev}$ to $(n + 0.24)\, f_{rev}$ in steps of $2 \times 10^{-3} f_{rev}$, where n is the integer tune and f_{rev} the revolution frequency which are listed in Table I. Through this frequency scan, we compute the amplitude of beam response and its phase. However, as the excitation strength is increased, it is observed that the response curves are different according to the direction of the frequency sweep, i.e., downward or upward [23, 24]. The driving amplitude should be applied as low as the response can be detected. In the simulations, the driving amplitude is chosen as $10^{-4}\ \sigma_{x',y'}$, where $\sigma_{x',y'}$ are the transverse rms slopes. Besides, the response profile is affected by the sweeping rate. A relaxation time needs therefore to be applied just before starting the evaluation of beam transfer function at each successive driving frequency, because the directional dependence of the response amplitude may be due to the remnants of nonlinear oscillations driven by former excitations. In order to avoid the uncertainty, we reload fresh particles with distribution identical to the initial one.

The response curve reveals two peaks, as shown in Fig. 10 (a) and (b): One peak is close to 0.230 which is the horizontal tune, and the other is 0.225 which is the vertical tune. The amplitude is in arbitrary units and normalized by the peak amplitude. We observe signs of transverse coupling in these BTFs, the vertical tune shows up as a lower peak in the horizontal BTF and similarly the horizontal tune appears in the vertical BTF. It is clear that due to resonance with the external force, the betatron amplitude of particles grows when the driving frequency is close to the betatron frequency. However, we observe valleys in the response at $\nu_d = 0.226$ and $\nu_d = 0.228$ for both horizontal and vertical amplitudes. They are located at the resonance line of order 9, and may stem from the detuning of particles away from the resonance. For a sinusoidal driving force, the phase of

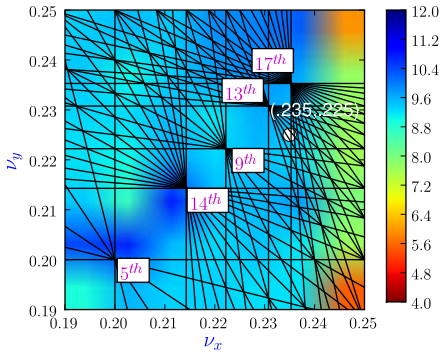

(a)

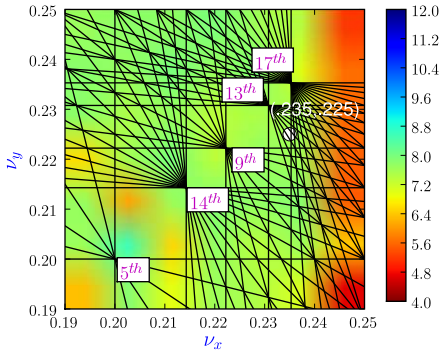

(b)

Figure 9: Tune scan of dynamic aperture at deuteron collision energy: (a) $d_y = 8\ \sigma$ and (b) $d_y = 6\ \sigma$. Working point $(28.235, 29.225)$ is plotted as a white dot. Red indicates low dynamic apertures while blue indicates high dynamic apertures. The unit of dynamic aperture is σ.

the beam transfer function change its sign through the resonance frequency [25]. Since the simulation does not account for the phase change due to cable delays between the pickup and the network analyzer, the absolute phases will not agree between simulations and measurements. We can however expect a similar phase variation across the resonance. Both simulation and measurement results show the flip of the phase angle as shown in Fig. 10 (c) and (d). The small differences in the zero crossing phase and the differences in peak locations of the amplitudes between simulation and measurement are likely due to the external impedances and the nonlinearities not included in the simulation.

The influence of the current carrying wire to the beam transfer function is presented through the comparison of Fig. 11 which shows the beam amplitude and phase response obtained without the wire and with the wire powered at 50A and at two separations in a deuteron beam study. The shift of a peak location of the amplitude increases as the wire separation decreases while the width of the amplitude response widens, as shown in Fig. 11 (a) and as expected from the increase in the size of the tune spread. The wire with 10 σ and 8 σ separations shifts the peak location of the horizontal response by 3.4×10^{-3} and 4.1×10^{-3} respectively, which are equivalent to the tune shift of zero amplitude particles. As shown in Fig. 11 (c), the wire moves the phase profile leftward commensurately with the shift of the amplitude. The BTF response contains a wealth of information about the beam, a detailed analysis of measured and simulated BTFs is left to a subsequent publication.

E. Diffusion Coefficients

We have calculated the beam diffusion due to nonlinear particle dynamics which includes the nonlinearities from the machine itself, the head-on beam-beam interactions, and the current carrying wire. Growth of particle amplitudes may be described by a diffusion in action variables. The diffusion coefficients can characterize the effects of the nonlinearities present in the accelerator, and can be used to find numerical solutions of a diffusion equation [26]. The solutions yield the time evolution of the beam density distribution function for a given set of machine and beam parameters. This technique enables us to follow the beam intensity and emittance growth for the duration of a luminosity store, something that is not feasible with direct particle tracking. Here we will focus only the calculation of the diffusion coefficients and compare them with past measurements in RHIC.

The transverse diffusion coefficients can be calculated numerically from

$$D_{ij}\left(a_i, a_j\right) = \frac{1}{N}\left\langle \left(J_i(a_i, N) - J_i(a_i, 0)\right) \left(J_j(a_j, N) - J_j(a_j, 0)\right)\right\rangle, \tag{5}$$

where $J_i\left(a_i, 0\right)$ is the initial action at an amplitude a_i, $J_i\left(a_i, N\right)$ the action at an amplitude a_i after N turns, $\langle\rangle$ the average over simulation particles, and (i, j) are the horizontal x or the vertical y coordinates. Equation (5) is averaged over a certain number of turns to eliminate the fluctuation in action due to the phase space structure, e.g. resonance islands. In the simulations, the tracking code evaluates the diffusion coefficients in two-dimensional action space with the boundary determined by the dynamic aperture obtained in the previous section. We load the initial particle distribution which is built by using 100 particles placed at the same transverse action. The tracking is performed for 10^6 turns. The diffusion coefficient is averaged every 10^4 turns at which the coefficient approaches approximately the asymptotic limit. The above process is performed over the transverse action space with the boundary typically set at an amplitude of 7 σ.

Figure 12 presents the contour plot of the horizontal and vertical components of the diffusion coefficients for the gold beam at collision energy. In these plots we ob-

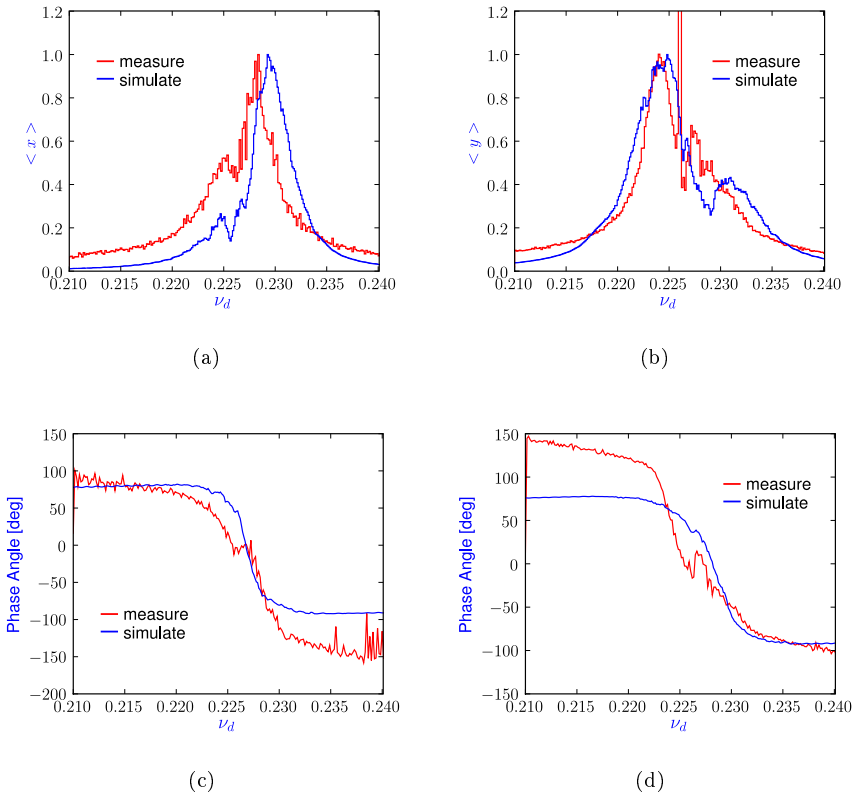

Figure 10: Amplitude of (a) horizontal and (b) vertical beam transfer functions, and phase angle of (c) horizontal and (d) vertical BTF for deuteron beam. The amplitude is in arbitrary units, and the phase angle is in degree. The wire strength is 125 Am.

serve that the diffusion coefficients have angular dependence. The horizontal diffusion D_{xx} depends strongly upon the horizontal action J_x while its dependence on the vertical action is weak. Similarly the vertical diffusion D_{yy} depends primarily on the vertical action. The diffusion coefficients scale exponentially with initial actions, specially at small actions, in both horizontal and vertical directions but at very different rates in each direction. A single exponential fit does not however suffice but a combination of at least two different exponentials is required to describe the growth of the diffusion coefficients from the origin to the dynamic aperture.

Figure 13 shows the diffusion coefficients for three RHIC situations: gold beam at store, deuteron beam at store, and proton beam at store. The coefficients are plotted at the action $J = \sqrt{J_x^2 + J_y^2}$ after averaging them at the same action and are compared with the measurements obtained by fitting the time-dependent loss rate after moving a collimator into and out from the beam [27]. The loss rate due to the movement of the collimator can be described by [28]

$$\begin{aligned} \dot{N}^{(1)}(t) &= a_0 \left(1 + \frac{\Delta z}{\sqrt{\pi R}\,(t - t_0)}\right) + a_1, \\ \dot{N}^{(2)}(t) &= a_0 \mathrm{erfc}\left(\frac{\Delta z}{\sqrt{\pi R}\,(t - t_0)}\right) + a_1, \end{aligned} \tag{6}$$

where the superscript (1) and (2) stands for the inward and outward movement of the collimator, Δz the change in z due to the collimator movement, R the diffusion coefficient, and a_0 and a_1 are constants. The diffusion coefficient R can be obtained directly from the fit of measured loss rates. In Fig. 13, the vertical axis is a logarithmic scale. It should be noted that dependence of diffusion coefficients on the initial action is exponential at small amplitudes and power law like at larger amplitudes. However, since the measured coefficients are fitted by a power law, i.e. $D \sim J^n$, they agree with simulations only at large actions. Since the collimators were not moved into the beam core, the diffusion coefficients were not measured at small actions. Conversely it is difficult to calculate the coefficients in simulations at large action because some of the particles are lost quickly. The effects of wire on diffusion coefficients are considerable at all action amplitudes, as shown in Fig. 13. For exam-

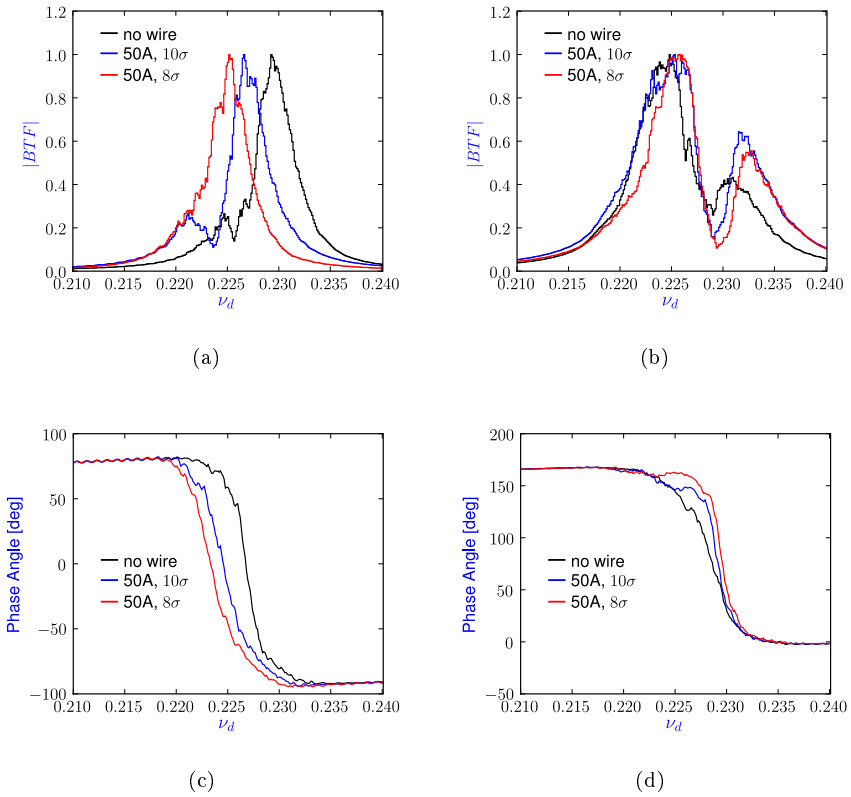

Figure 11: Amplitude of (a) horizontal and (b) vertical beam transfer functions, and phase angle of (c) horizontal and (d) vertical BTF for deuteron beam. The amplitude is in arbitrary units, and the phase angle is in degree. The wire current is set 50A. The separation is in unit of rms beam size at wire location.

ple, the diffusion coefficient at 3 σ amplitude becomes 20 times larger when the wire with strength 125 Am and separation $d_y = 8\ \sigma$ is applied. First we observe that the relative increase of diffusion coefficients at below 3 σ amplitude for the deuteron beam is higher than that for the gold beam. In general the diffusion process depends on the particle motion in phase space and the resonance structure due to the nonlinearities. The differences in tunes change the cross-talk between the different nonlinearities as well as the resonance driving terms which are likely to be responsible for the differences in diffusion. The enhanced diffusion at near 3 σ amplitude for the deuteron beam leads to significant increase of particle loss under the simulation conditions (see the following section).

F. Beam losses as a function of wire-beam separation

The beam lifetime in RHIC is determined by the inelastic interactions and beam-beam interactions when the beams are in collision as well as nonlinearities of machine elements, intra-beam scattering and residual gas scattering. In this section we will focus on the impact of the wire on the beam loss rates as the beam-wire separation is changed. In this study, the initial beam distribution is a hollow Gaussian in transverse phase space and a normal Gaussian in longitudinal phase space. The initial transverse beam sizes are obtained from the RHIC optics and typical initial emittances while the bunch length is taken from measured values.

The tracking is done with 5×10^3 macroparticles, and carried out over 10^7 turns for each wire separation. The loss rates are estimated from the asymptotic limit by extrapolating the simulated loss rate from 10^7 turns to infinity as shown in Fig. 14. It is observed that in the beginning of the simulation, the loss rate decreases exponentially rapidly and then approaches a constant rate at later times. We apply, therefore, an exponential decay fit, i.e., $ae^{-t/\tau} + b$, to the loss rate data between 4×10^6 and 1×10^7 turns. The asymptotic loss rate is the parameter b.

Figure 15 plots the asymptotic beam loss rate due to the wire as a function of beam-wire separation distance for the case of Table I. For the gold injection energy study, we include the chromaticity correcting sextupoles, chromaticity set to two units, and the wire. It can be seen in Fig. 6 (a) that the electromagnetic force of the wire decreases the dynamic aperture significantly compared to

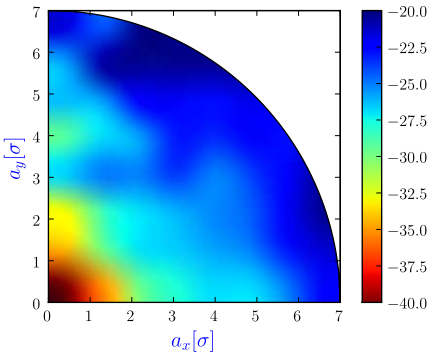

(a)

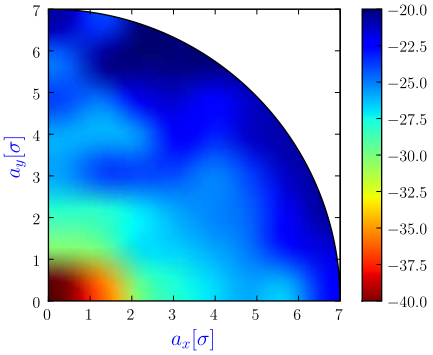

(b)

Figure 12: Contour plot of (a) the horizontal diffusion coefficient D_{xx} and (b) the vertical diffusion coefficient D_{yy} for gold beam at collision energy. The coefficients are calculated at the Blue ring. The color assignment is logarithmically scaled in the plots.

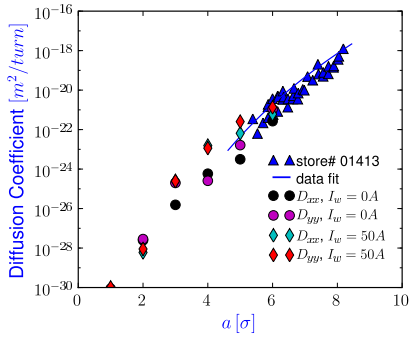

(a)

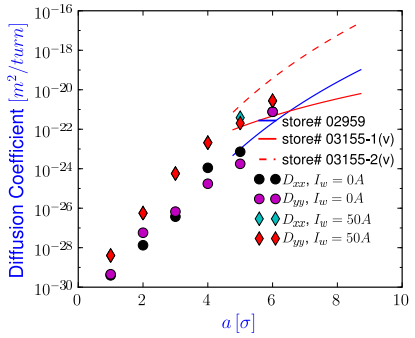

(b)

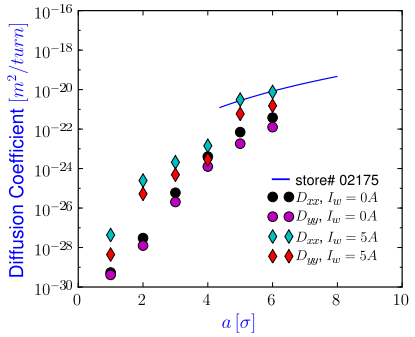

(c)

Figure 13: Plot of diffusion coefficients of (a) gold, (b) deuteron, and (c) proton stores of RHIC. The coefficients are calculated at the Blue ring. The wire-beam separation distance is 8 σ at a wire location. The coefficients were measured and fitted in stores in previous years [27].

the case when the wire is not present. The particle loss rate of the beam shows a sharp increase wire separations smaller than 8 σ.

For the collision energy simulations, we include the nonlinear field errors in the triplets, the head-on beam-beam interactions, and the nonlinearities in the injection energy study. The onset of beam losses, seen in Fig. 15 (b) and (c), is observed at 8 σ and 9 σ for gold and deuteron beams respectively. In all three cases, the threshold separation for the onset of sharp losses observed in the measurements and simulations agree to better than 1 σ. It is also significant that the simulated loss rates at 7 and 8 σ separation for the gold beam and 8 and 9 σ for the deuteron beam are very close to the measured loss rates. At fixed separation, the wire causes a much higher beam loss with the deuteron beam than with the gold beam. For example, the loss-rate for the gold beam at a 8 σ separation is about 10 %/hr while for the deuteron beam the loss rate is about an order of magnitude higher both in measurements and simulation. This difference is not reflected in the dynamic apertures, shown in Figure 6, which are about the same for the two cases at the same beam-wire separation. Nor is this difference correlated to the tune footprint and the resonance lines, seen in Fig. 3, where the footprint for the deuteron beam is free of resonance lines lower than the 12^{th} while the gold footprint is spanned by the 9^{th} and 12^{th} order resonances. However the frequency diffusion maps with the wire, seen in Fig. 4 and Fig. 5, show greater diffusion in the deuteron case than in the gold case. This correlation of the frequency diffusion maps with the loss rates observed here deserves to be studied more deeply

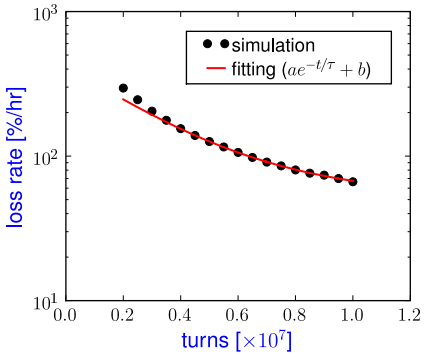

Figure 14: Plot of the variation of loss rate versus the number of tracking turns. The loss rate is estimated from the asymptotic value of the exponential decay fit, i.e., $ae^{-t/\tau}+b$.

	gold beam injection	gold beam store	deuteron beam
Measurement	-5.2	-7.3	-9.4
Simulation	-14.2	-11.9	-11.2

Table II: Dependence of loss rate on the beam-wire separation: The loss rates are fitted to $\tau \propto d_y^{\alpha}$, where d_y is the separation, and the power α is listed on the table.

and tested for validity in other accelerators. The action diffusion seen in Fig. 13 is also larger in the deuteron beam than the gold beam at small amplitudes by one to two orders of magnitude. Thus both frequency and action diffusion seem to be better correlated with loss rates than the traditional short term indicators like footprints and dynamic aperture.

Changing the beam-wire separation changes several parameters including the tunes, the tune spread, the resonance driving terms etc. The wire separation alone cannot describe the change in the dynamics that influences the loss rates. Nonetheless the loss rates seen in Fig. 15 can be fitted to a power law in the separation. The results for the three cases for the measurements and simulations are shown in Table II. The simulations have studied smaller separations than would be practical in RHIC - the large loss rates seen at the smallest separation would have quenched the machine. However, the simulations show the steep climb in the loss rate beyond a threshold separation and consequently will have a higher power law behavior. The power law at injection is somewhat higher than at collision but the power laws for gold and deuteron beams are very close despite the large difference in loss rates. We expect that the power laws depends on the details of the machine and not to be universal. In fact different power laws have been reported for the SPS and the Tevatron [8, 29, 30].

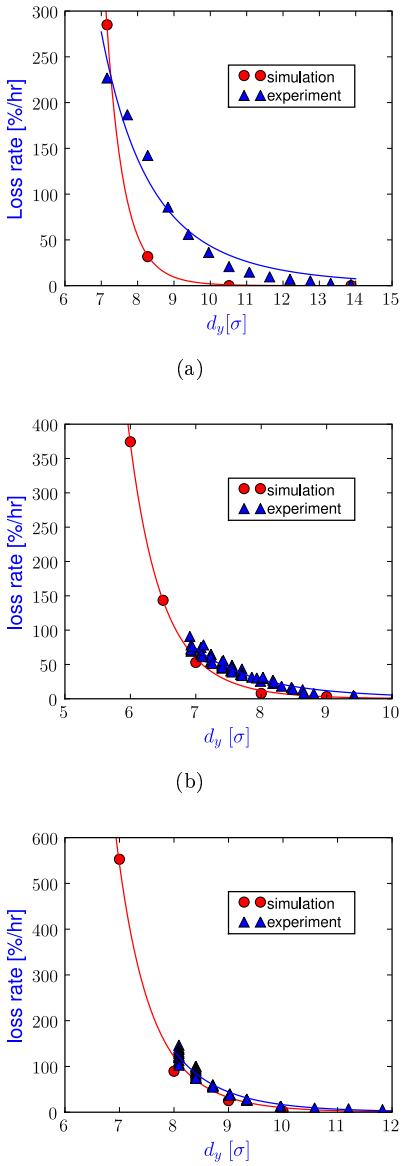

(a)

(b)

(c)

Figure 15: Comparison of the simulated beam loss rates with the measured as a function of separations. (a) gold beam at injection energy, (b) gold beam at collision energy, (c) deuteron beam at collision energy. Wire strength is 125 Am.

V. SUMMARY

In order to study the effects of the machine nonlinearities and the beam-beam interactions, including strong localized long-range beam-beam interactions, we have developed a six-dimensional weak-strong code `BBSIMC`. Machine nonlinearities, beam-beam collisions and the field of a current carrying wire can be included in the model.

We have studied the effects of the wire on the beam dynamics in three different cases: gold beam at injection,

gold beam at store, and deuteron beam at store. Results show that the betatron tune change due to the wire is well tracked by the simulation, and that the stability of particle motion is strongly influenced by the wire which causes a significant increase in tune spread and diffusion for both gold and deuteron beam. Tune diffusion with the gold beam and the wire is appreciable only at amplitudes larger than 2 σ while the tune diffusion with the deuteron beam and the wire is significantly larger extending to the beam core at amplitudes down to 0.5 σ.

At injection energy, the dynamic aperture is largely determined by the wire, while the wire and the IR multipoles have a major impact on the stability boundary at collision. With the beam-wire separation only along the vertical axis, it is found that the stability boundary near the vertical axis is linearly proportional to the beam-wire separation. We observe, from the tune scan of dynamic aperture, that at injection the largest and the smallest dynamic apertures are distributed along a band parallel to the zone along $\nu_x - \nu_y \simeq 0.02$ and $\nu_x - \nu_y \simeq 0.03$ respectively at all wire separations while at collision the largest dynamic apertures are distributed nearly along the diagonal between $\nu_x = 0.21$ and $\nu_x = 0.24$. By modeling the stripline kicker we obtain the amplitude and phase angle of the transverse BTF. Results show that the betatron tune is well identified by the simulation, and that the wire changes characteristics of the beam response significantly in the horizontal plane, similar to the result for the tune shift.

In simulations the wire enhances the diffusion. This effects is particularly pronounced in the plane of the wire, and at amplitudes of about 3 σ, where the wire can increase the diffusion rate by more than an order of magnitude. The action diffusion for the deuteron beam is larger than for the gold beam, similar to the result for frequency diffusion. Simulations of the beam loss rate when the wire is present are in good agreement with the experimental observations. The threshold separation at which there is a sharp rise in the loss rates agree to better than 1 σ. The loss rates with the deuteron beam are found in measurements and simulations to be nearly an order of magnitude higher than with the gold beam. Comparisons of tune footprints and dynamic apertures of these two cases show no indication that the loss rates may be higher with the deuteron beam and in fact the tune footprint with the deuteron beam is free of low order resonances. However frequency diffusion and action diffusion with the deuteron beam are substantially higher than with the gold beam implying that these diffusion measures may be better indicators of loss rates.

In this paper simulation results of the beam-wire interactions were compared with measurements taken when the long-range beam-beam interactions were not present. It is expected that compensation of parasitic interactions using the wires will be tested during the RHIC run in 2009. We plan to compare simulations with these forthcoming experimental results and also to determine the effectiveness of the compensation of long-range interactions in the LHC.

Acknowledgments

We thank Y. Luo and R. Calaga for help with the RHIC lattice. V. Boocha, B. Erdelyi and V. Ranjbar made significant contributions to the development of the code. Some of the parallel computations were performed at the NERSC facility at LBL. This work was supported by the US-LARP collaboration which is funded by the US Department of Energy.

[1] T. Sen, B. Erdelyi, M. Xiao, and V. Boocha, Phys. Rev. ST Accel. Beams **7**, 041001 (2004).

[2] V. Shiltsev, Y. Alexahin, V. Lebedev, P. Lebrun, R. S. Moore, T. Sen, A. Tollestrup, A. Valishev, X. L. Zhang, Phys. Rev. ST Accel. Beams **8**, 101001 (2005).

[3] J.P. Koutchouk, LHC Project Note 223, CERN (2000).

[4] J.P. Koutchouk, J. Wenninger, and F. Zimmermann, in *Proceedings of the 9th European Particle Accelerator Conference, Lucerne, 2004* (EPS-AG, Lucerne, 2004), p. 1936.

[5] U. Dorda, J. Koutchouk, R. Tomas, J. Wenninger, F. Zimmermann, R. Calaga and W. Fischer, in *Proceedings of the 11th European Particle Accelerator Conference, Genoa, 2008* (EPS-AG, Genoa, Italy, 2008), p. 3176.

[6] C. Milardi, D. Alesini, M.A. Preger, P. Raimondi, M. Zobov, and D. Shatilov, in Proceedings of CARE-HHH-APD IR'07 Workshop (Frascati, Italy, 2007) p. 92.

[7] W. Fischer, et al., in *Proceedings of the 2007 Particle Accelerator Conference, Albuquerque, New Mexico, 2007* (IEEE, Albuquerque, New Mexico, 2007), p. 1859.

[8] F. Zimmermann, J.-P. Koutchouk, F. Roncarolo, J. Wenninger, T. Sen, V. Shiltsev, and Y. Papaphilippou, in *Proceedings of the 2005 Particle Accelerator Conference, Knoxville* (IEEE, Piscataway, NJ, 2005), p. 686.

[9] URL `http://www.c-ad.bnl.gov/APEX/APEX2008/`.

[10] K. Hirata, H. Moshammer, and F. Ruggiero, Particle Accel. **40**, 205 (1993).

[11] B. Erdelyi and T. Sen, Tech. Rep. Fermilab-TM-2268-AD, Fermilab (2004).

[12] C.K Birdsall and A.B. Langdon, *Plasma Physics via Computer Simulation* (McGraw-Hill, New York, 1985).

[13] URL `http://www-ap.fnal.gov/~hjkim`.

[14] MPI-2: Extensions to the Message-Passing Interface, Message Passing Interface Forum, U. of Tennessee, Knoxbille, TN (2003).

[15] S. Balay, W.D. Gropp, L.C. McInnes, and B.F. Smith, Tech. Rep. ANL-95/11 - Revision 2.3.3, ANL (2008).

[16] *HDF5 User's Guid*, NCSA, UIUC, Urbana, IL (2005).

[17] F. Zimmermann, Tech. Rep. LHC Project Report 502, CERN (2001).

[18] W. Fischer, R. Alforque, H.C. Hseuh, R. Lambiase, C.J. Liaw, G. Miglionico, T. Russo, J.-P. Koutchouk, F. Zimmermann, and T. Sen, Tech. Rep. BNL C-A/AP/236, BNL (2006).
[19] J. Laskar, Physica D **67**, 257 (1993).
[20] J. Borer, G. Guignard, A. Hofmann, E. Peschardt, F. Sacherer, and B. Zotter, IEEE Trans. Nucl. Sci. **NS-26**, 3405 (1979).
[21] P. J. Chou and G. Jackson, in *Proceedings of the Particle Accelerator Conference, Dallas, TX, 1995* (IEEE, New York, 1995), p. 3088.
[22] V. Kornilov, O. Boine-Frankenheim, W. Kaufmann, and P. Moritz, Tech. Rep. GSI-Acc-Note-2006-12-001, GSI Darmstadt (2006).
[23] M.G. Minty and Frank Zimmermann, Tech. Rep. SLAC-PUB-7467, SLAC (1997).
[24] J. M. Byrd, W.-H. Cheng, and F. Zimmermann, Physical Review E **57**, 4706 (1998).
[25] A. W. Chao, Physics of Collective Beam instabilities in High Energy Accelerators (John Wiley & Sons, 1993).
[26] H. J. Kim, T. Sen, N.P. Abreu, and W. Fischer, in *Proceedings of EPAC08* (Genoa, Italy, 2008), p. 3119.
[27] R.P. Fliller, Ph.D. thesis, Stony Brook University (2004).
[28] M. Seidal, Ph.D. thesis, Universität Hamburg (1994).
[29] P. Lebrun, T. Sen, V. Shiltsev, X.L. Zhang, and F. Zimmermann, Tech. Rep. AB-Note-2004-041 MD, CERN (2004).
[30] U. Dorda, R. Calaga, W. Fischer, J.P. Koutchouk, R. Tomas, J. Wenninger, and F. Zimmermann, Tech. Rep. LHC Project Report 1102, CERN (2008).